Gold nanoparticle chains

Julien Vieaud, Jie Gao, Jérémy Cane, Michel Stchakovsky, Aotmane En Naciri, Katsuhiko Ariga, Reiko Oda, Emilie Pouget, Yann Battie

Gold Nanoparticle Chains: Synthesis, Characterization, and Modeling Using Spectroscopic Ellipsometry

Julien Vieaud, Jie Gao, Jérémy Cane, Michel Stchakovsky, Aotmane En Naciri, Katsuhiko Ariga, Reiko Oda, Emilie Pouget, and Yann Battie

In this paper, we explore the ability of ellipsometry to characterize colloidal suspensions composed of gold nanoparticle (NP) chains. The complex effective index of these suspensions is deduced from ellipsometric measurement by using a wavelength-by-wavelength inversion without any dispersion law. We show that the effective refractive index of these colloids is defined by the nature of the solvent, whereas their effective extinction coefficient is mainly sensitive to the plasmonic properties of NP chains. The influence of the NP radius distribution and arrangement on the effective extinction coefficient of NP chain are investigated through simulations based on the coupled point dipole method (CDM). We clearly show that this coefficient is mainly sensitive to the interparticle distance and the number of NPs in the longest segment of chains. We demonstrate that the distribution of the number of NPs in the longest segment of chains and their volume fractions can be directly deduced from the ellipsometry by using the CDM.

Introduction

Metallic nanoparticles (NPs) such as gold NPs (Au NPs) show attracted plasmonic properties, which come from the collective oscillations of their free electrons. (1) This process is resonant at a particular frequency of light and is responsible for the bright intense colors of metallic NP suspensions. The characteristics of plasmon resonance mainly depend on the NP size, shape, and environment. (2−6) These NPs, which act as nanoantennas, can be used to manipulate light–matter interactions at the nanoscale. (7,8) Thus, metallic NPs can be viewed as building block elements of complex plasmonic nanostructures (9) such as helices, (10−13) oligomers, (14−18) or NP chains, (19−24) which exhibit unconventional optical properties. Indeed, NPs are strongly coupled in self-assembled NP chains, resulting in an enhancement of the electric field in the gap between adjacent NPs. (25) These self-assembled NP chains are attractive candidates for the amplification of the Raman signals, (26,27) optical communications, (28−30,39) and sensors. (31,32)

Conventional NP synthesis routes and self-assembly techniques, used to produce colloidal suspension composed of NP chains, unavoidably conduct to NP chains showing size polydispersity, disorder, and ramifications which could have strong impacts on their optical properties. (21−23,33) It is therefore crucial to develop models to correlate the morphology of interacting NP chains with their optical properties. This can be simulated in the framework of generalized Mie theory, discrete dipole approximation, T-matrix approach, or boundary element method. (34−38) These electromagnetic approaches take into account the multipolar effect. Other approaches such as time-dependent local density approximation or quantum-corrected model (39,49) can be introduced to simulate quantum effects such as charge-transfer plasmon or tunneling effects, which occur for small interparticle distance. (41−45) However, all of these approaches require large computing resources especially for large structure or for small interparticle distance. In addition, these complex approaches hide the information about the physical meaning of the spectral response of plasmonic systems. This prohibits their use to simulate the optical properties of colloidal suspensions composed of long NP chains with

some distributions, disorder, and ramifications. In this context, coupled point dipole method (CDM), (10) which considers each NP as a dipole, can be considered as a tradeoff to describe the optical properties of these colloids with accessible computing resources, despite the fact that it cannot take into account multipolar interaction or quantum effects. Indeed, we have previously used this approach to give straightforward information concerning the circular dichroism of nanohelices composed of interacting gold NPs and showed that this method is suitable for designing an optimized nanostructure architecture. (10)

The topology of self-assembly nanostructures is usually characterized by transmission electron microscopy (TEM) in dried or in cryo modes. Because conventional TEM only gives a two-dimensional projection of three-dimensional nanostructures, the nanostructure topology can be misestimated. In addition, TEM observation in the tomography mode is too time-consuming to record the distribution of topologic defects over a significant number of nanostructures. Thus, the development of nonlocal characterization tools is required to characterize self-assembled nanostructures. Small-angle X-ray scattering was previously used to determine the crystalline structures of self-assembled Au NPs. (46) However, this technique requires some facilities such as synchrotron beam line and is not sensitive to the optical properties of nanostructures. Spectroscopic ellipsometry is an indirect optical characterization tool based on the change of the polarization state of light after reflection on the sample. (47) On contrary to the standard transmission spectroscopy, ellipsometry is sensitive to both the real part and the imaginary part of the complex refractive index of materials. This technique, which requires an appropriate modeling, enables the determination of the effective refractive index of nanostructured materials and the optical properties of the matrix. In other words, ellipsometry gives a complete characterization of the optical properties of the nanocomposite. We have recently developed an ellipsometric cell to characterize the optical properties of colloids. (48) In this work, the recorded ellipsometric spectra were analyzed with the shape distributed effective medium theory (SDEMT) in order to determine the shape distribution of Au nanorods in water. However, because the SDEMT theory fails to describe the interaction between NPs, the ellipsometric measurement was restricted to colloidal solutions composed of isolated NPs. (48)

In the present paper, we explore further the ability of ellipsometry to characterize colloidal suspensions composed of Au NP chains. The complex effective index of these suspensions is deduced from ellipsometric measurement by using a wavelength-by-wavelength inversion without any dispersion law. (47) We show that the real part of the complex refractive index can be assimilated to the refractive index of the matrix, whereas the imaginary part is sensitive to the plasmonic properties of NP chains. Thus, this is the first report, to the best of our knowledge, on the influence of the NP radius distribution and arrangement on the effective extinction coefficient of NP chain through simulations based on the CDM. We conclude that the distribution of the number of NPs per chains can be determined from ellipsometric spectra by analyzing them with the CDM model without any assumption concerning the optical properties of the matrix.

Materials and Methods

Synthesis of S1 to S6 Au NP Suspension

1/Synthesis of 14 nm diameter Au NPs, following the protocol described by Ji et al. (49)

The auric acid ($HAuCl_4 \cdot 4H_2O$; M = 411.85 g·mol–1; CAS: 16961254), sodium tricitrate ($C_6H_5Na_3O_7,2H_2O$; M = 294.1 g·mol–1; CAS: 6132043), and polyacrylic acid (PAA) with Mw = 5000 g·mol–1 were purchased from Sigma-Aldrich. The auric acid solution (0.492 mL, c = 0.486 mol/L) and sodium tricitrate solution (6 mL, c = 0.145 mol/L) are added to 500 mL of hot water under stirring,

and the solution is kept heating for 30 min. A suspension of 14 nm diameter Au NPs in water is obtained with a volume fraction of 2.4 × 10–6.

These Au NPs are then stabilized with PAA inspired by the protocol of Schneider and Decher. (50) The pH of the Au NP solution is adjusted to 4 (with HCl 0.1 M solution) to which 1.5 g of PAA is added; then, the solution is rapidly plunged into a sonication bath. The solution is then stirred overnight at room temperature. Finally, the pH of the solution is increased to 7 (with NaOH 1 M solution) and washed by water using centrifugation to replace the excess of PAA. The solution is then concentrated or diluted to obtain a volume fraction of 2.5 × 10–5.

2/Destabilization of the Au NP suspension with HCl 10 mM to obtain the colloidal suspensions S1 to S6:

The total volume of each solution is 4 mL, and volume fraction of gold is maintained at φ = 0.78 × 10–5. The synthesis was done in glass flasks. The water and HCl were mixed first, to which Au NP suspensions were added in one shot and the flasks were shaken on a shaker plate at 800 rpm for 1 h and 30 min and let to rest at room temperature for 24 h. Volumes and pH of the different solutions are summarized in Table 1. The colors of the solutions evolve from red to blue (Figure 1)

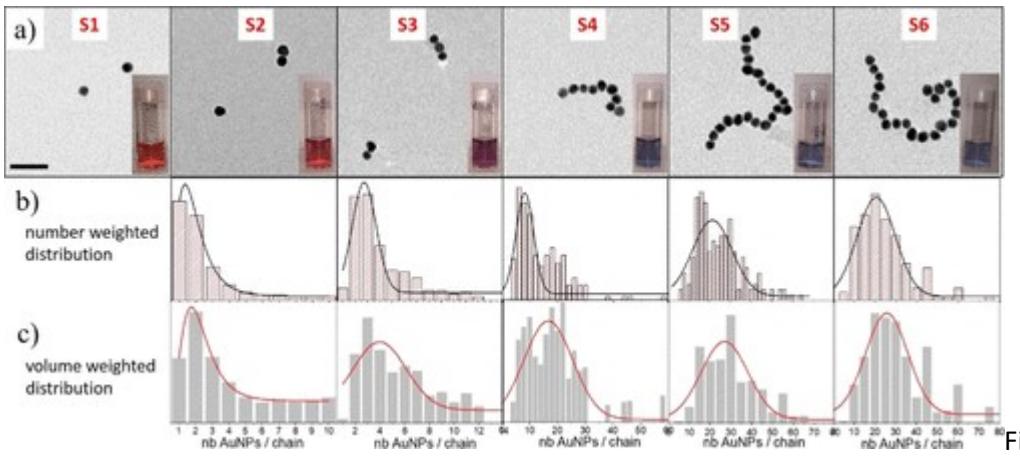

Figure 1

Figure 1. (a) TEM images of S1 to S6 Au NP chains (pH is 8.5, 4.29, 4.19, 4.09, 3.93, and 3.90, respectively). Scale bare = 50 nm. In the inset: pictures of the samples showing the color evolution. (b) Number-weighted and (c) volume-weighted distributions of the number of Au NPs in the longest segment of chains contained in S2 to S6 suspensions, determined from TEM images (from 129 to 200 measurements).

Table 1. Composition and pH of Au NP Suspensions

	S1	S2	S3	S4	S5	S6
$V_{Au\ NPs\ (\phi=2.5\times10^{-5})}$ (µL)	1250	1250	1250	1250	1250	1250
$V_{HCl\ 10mM}$ (µL)	0	95	100	105	110	115
V_{H_2O} (µL)	2750	2655	2650	2645	2640	2635
pH	8.5	4.29	4.19	4.09	3.93	3.90

TEM Observation

TEM was performed at room temperature on a Philips EM 120 electron microscope operating at 120 kV, and the images were collected by a 2k × 2k Gatan ssCCD camera. Drops of diluted dispersions of the hybrids were deposited on carbon films coated 200/400 mesh copper grids. The excess of liquid was blotted with a filter paper.

CryoTEM Observation

The solutions were deposited on Lacey F/C 300-mesh copper grids after glow discharge inside a Vitrobot Mark IV chamber set to 100% relative humidity. Blotting and vitrification were done automatically with the robot. Observation was performed at −170 °C on a FEI Technai-F20 200kV-FEG electron microscope, and the images were collected by a 4k × 4k FEI Eagle camera.

Ellipsometric Measurements

Ellipsometric measurements were recorded at room temperature with a phase modulation ellipsometer (UVISEL, HORIBA Jobin Yvon) in the 275–830 nm range. As we have shown previously, this ellipsometer, which uses fixed polarizing elements, is required for accurate measurements on liquids. (48) Two ellipsometric parameters Is and Ic which depend on the ellipsometric angles Ψ and Δ, respectively, are measured

$$I_s = \sin 2\Psi \sin \Delta \quad (1)$$

$$I_c = \sin 2\Psi \cos \Delta \quad (2)$$

A specific liquid cell (48) was used for ellipsometric measurements on liquids. Briefly, the liquid under study is sandwiched between the base of an isosceles silica prism with an angle of 55° and a silicon wafer. This ensures the absence of surface waves at both interfaces of the liquid. The thickness of the liquid is fixed at 400 µm by electro-polished Ni blades spacers. As we have shown previously, (48) this thickness is sufficiently high to detect NPs at the parts per million by volume (ppmv) level. Two beams are collected by the optical fiber of the ellipsometer: (48) the beam reflected at the prism/liquid interface and the beam which comes from the first reflection at the liquid/silicon substrate interface.

Because ellipsometry is an indirect characterization tool, a model is required to exploit the ellipsometric measurements. This model consists of a silicon substrate covered by a 3 nm silicon oxide layer and a 400 µm liquid layer. Silica is used as ambient. The angle of incidence of light, defined by the angle of the prism is 55°. By considering the coherence length of the ellipsometer, estimated at 34 µm, the modeling is made according to the incoherent reflection condition as reported in our previous work. (48) Indeed, the ellipsometric parameters Is and Ic are calculated

from the Fresnel coefficients rp and rs of the Si/SiO2/liquid/prism system for p and s polarized light, respectively

$$I_s = \frac{2\,\mathrm{Im}(r_p r_s^*)}{|r_p|^2 + |r_s|^2} \quad (3)$$

$$I_c = \frac{2\,\mathrm{Re}(r_p r_s^*)}{|r_p|^2 + |r_s|^2} \quad (4)$$

where

$$|r_p|^2 = |r_{p01}|^2 + |t_{p01}|^2 |t_{p10}|^2 |r_{p123}|^2\, e^{-4\mathrm{Im}(\beta)} \quad (5)$$

$$|r_s|^2 = |r_{s01}|^2 + |t_{s01}|^2 |t_{s10}|^2 |r_{s123}|^2\, e^{-4\mathrm{Im}(\beta)} \quad (6)$$

$$r_p r_s^* = r_{p01} r_{s01}^* + t_{p01} t_{p10} r_{p123} t_{s01}^* t_{s10}^* r_{s123}^*\, e^{-4\mathrm{Im}(\beta)} \quad (7)$$

$$\beta = 2\pi \frac{h}{\lambda} n_1 \cos\theta_1 \quad (8)$$

where h = 400 μm and θ1 are the thickness of the colloid layer and the angle of refraction of light in this layer, respectively. ri01, ti01, and ti10 (i = p, s) are the reflection and the transmission Fresnel coefficients at the prism/liquid interface. ri123 (i = p, s) is the reflection Fresnel coefficient of the Si/SiO2 substrate, considering the liquid as the ambient. The complex effective refractive index of the suspensions (N = n + iκ) is determined from ellipsometric measurements according to a wavelength-by-wavelength numerical inversion (47) which consists of the minimization of the root-mean-square error between the measured and calculated ellipsometric parameters Is and Ic at each wavelength by using the Levenberg–Marquardt algorithm. (51)

Coupled Point Dipole Method

The extinction coefficient of suspension, which contains chains of spherical NPs, is calculated by using the CDM. In this approach, each spherical NP m has a sufficiently small radius Rm to be considered as a point dipole which has a polarizability αm defined by (10)

$$\alpha_m = {R_m}^3 \frac{\varepsilon_{np}(R_i) - \varepsilon_h}{\varepsilon_{np}(R_i) + 2\varepsilon_h} \quad (9)$$

where εh is the dielectric function of the solvent and εnp(Rm) the dielectric function of the Au NP m. By considering a classical approach, this latter can be calculated by taking into account the confinement effect (1)

$$\varepsilon_{np}(R_m) = \varepsilon_{np}(\infty) - \frac{{\omega_p}^2}{\omega(\omega + j\Gamma_0)} + \frac{{\omega_p}^2}{\omega\left(\omega + j\left(\Gamma_0 + \frac{v_f}{R_m}\right)\right)} \quad (10)$$

εnp(∞) is the bulk dielectric function of gold given by Johnson and Christy, (52) ωp = 8.8 eV is the plasma frequency, Γ0 = 0.081 eV is the damping parameter, and vf = 1.4 × 106 m·s–1 is the Fermi velocity of free electrons of gold. The confinement effect, which limits the mean free path of conduction electrons, plays a major role for the NP radius smaller than 5 nm. (1,2)

Exposed to a local electric field , the NP m acquires a dipole moment given by

$$\overrightarrow{P_m} = \alpha_m \overrightarrow{E_{\mathrm{loc},m}} \quad (11)$$

We then considered that the NPs in a chain are coupled each other through a dipolar interaction. Indeed, the neighboring NPs (l) can be considered as nanoantennas, which radiate an electromagnetic field. The local electric field view by the NP m is the sum of the incident electric field () and the field generated by the other NPs l

$$\alpha_m^{-1}\overrightarrow{P_m} = \overrightarrow{E_{\mathrm{inc},m}} - \sum_{l \neq m}^{N_{\mathrm{np}}} A_{ml}\overrightarrow{P_l} \quad (12)$$

where Nnp is the number of NPs in the chain. In the following, we assume that the incident field is a linearly polarized plane wave

$$\overrightarrow{E_{\mathrm{inc},m}} = \overrightarrow{E_0}\, e^{j\overrightarrow{k}\,\overrightarrow{r_m}} \quad (13)$$

$\vec{k}$ is the wave vector, is the amplitude vector of the incident electric field, and is the position vector of the NP m.

The second term of eq 12 described the dipolar interaction between NPs. This term is expressed as

$$A_{ml}\overrightarrow{P_l} = \frac{e^{jkr_{ml}}}{r_{ml}^{3}}\left\{k^2 \overrightarrow{r_{ml}}\Lambda\overrightarrow{r_{ml}}\Lambda\overrightarrow{P_l} + \frac{1 - jkr_{ml}}{r_{ml}^{2}}\left(r_{ml}^{2}\overrightarrow{P_l} - 3\overrightarrow{r_{ml}}\cdot(\overrightarrow{r_{ml}}\cdot\overrightarrow{P_l})\right)\right\} \quad (14)$$

where and k are the norm of the wave vector $\vec{k}$. The first and the second terms of eq 14 describe the far- and near-field interactions, respectively. By applying the same procedure for all Au NPs, we obtain a set of 3Nnp linear equations, which can be rewritten as following (10)

$$AP = E_{\mathrm{inc}} \quad (15)$$

P and Einc are the 3Nnp dipole moment and incident electric field vectors, respectively. A is a tensor which describes the optical and geometrical properties of the NP assembly. The 3 × 3 off-diagonal block elements Aml of this tensor are deduced from eq 14, whereas the 3 × 3 diagonal block elements Amm are given by

$$A_{mm} = \alpha_m^{-1} I_{3,3} \quad (16)$$

I3,3 is the 3 × 3 identity matrix. The vector P is determined by solving eq 15 using the generalized minimal residual method. For a given incident electric field, the extinction coefficient of a suspension composed of GNP chains is calculated by

$$\kappa = \frac{2\pi}{|E_0|^2} C \sum_{m=1}^{N_{\mathrm{NP}}} \mathrm{Im}\left(\overrightarrow{E_{\mathrm{inc},m}}\,\overrightarrow{P_m}^{*}\right) \quad (17)$$

|E0| is the amplitude of the incident electric field, and C is the concentration of NP chains in the suspension. The extinction coefficient per number of NPs in a chain is given by

$$\kappa_c = \frac{\kappa}{N_{\mathrm{NP}} C} \quad (18)$$

In the following, we consider that the NP chains are randomly oriented in suspensions. To take into account these random orientations, the extinction cross section is averaged over 30 different orientations of the wave vector and polarization of the incident light according to the procedure described in our previous work. (10)

Results and Discussion

Representative TEM images of NP suspensions are shown in Figure 1a. For the solutions S1–S6, the Au NP volume fraction is fixed to be 0.78 × 10–5 and the pH of the solvent is varied from 8.5 to 3.9. The chain length distributions, evaluated by counting the number of NPs contained in the longest segment of each chain, are also reported in Figure 1b (distribution done on a number of measurements comprising between 130 and 200). Between pH 8.5 and 4.3, the spherical NPs remain individualized in solution as it is shown in Figure 1a (S1, pH 8.5). The radius of the NPs follows a Gaussian distribution with a mean value and standard deviation estimated at 7 and 0.5 nm, respectively (Figure S1). These NPs assemble to form chains for the pH < 4.3 (Figure 1a, S2–S6). In order to confirm that the chain formation is not a drying artifact during the TEM grid preparation, the solutions have also been observed in the hydrated state by cryoTEM and the interparticle gap g, defined as the distance between the surfaces of adjacent NPs, has been evaluated at 1.2 nm with a standard deviation of 0.2 nm. A cryoTEM image of the S4 sample and the interparticle gap distribution are shown in the Supporting Information (Figure S2). It has to be noted that the interparticle gap measured on the dry TEM images is only of 0.6 nm with a standard deviation of 0.3 nm, suggesting a shrinkage of the PAA chains during the drying of the samples on the TEM grids. Nevertheless, the morphology of the GNP chains and the number of particles per chain remain exactly the same in dried or hydrated state so the chain lengths can be evaluated by using the number of GNPs obtained from the statistics from the dry TEM images as the length unit. S2 (pH 4.29) and S3 (pH 4.19) are mainly composed of linear chains with less than 10 NPs (Figure 1a,b). At pH lower than 4.3, the chains get much longer, that is, >10 NPs, and ramifications appear in the S4 (pH 4.09), S5 (pH 3.93), and S6 (pH 3.90) suspensions. We observe from TEM image statistics that S4 chains contain about 2 ramifications, whereas S5 and S6 chains have about 3 ramifications.

The solution colors go from red for the number of NPs <5 to blue for longer chains (the number of NPs > 10, Figure 1). For pH lower than 3.9, the Au NPs totally aggregate and precipitate, showing the fragile equilibrium between the different forces inducing the chain formation.

The chain length distribution has been evaluated by counting the number of particles in the longest segment of each chain. Figure 1b shows the original measurements, and Figure 1c shows the same measurements plotted versus the volume occupied by the chains, which can directly be compared with the distributions obtained from ellipsometry. Indeed, the macroscopic polarization of a medium, that is, its optical response, is directly proportional to the volume density of the dipoles. As shown by eq 17, the extinction coefficient of colloidal suspension is proportional to the product between the volume and the concentration of the NP chains. The mean value of the number of NPs per chains gradually increases from 2 to 26 NPs as the pH of water varies from 4.29 to 3.9 (the values of the average number of particles per chain and the standard deviation are, respectively, for S2 to S6: 1.7 ± 0.5; 2.7 ± 0.9; 8 ± 3; 21 ± 9; and 20 ± 9 or 2.0 ± 0.4; 4 ± 2; 17 ± 8; 27 ± 11; and 26 ± 10). It is known that, in the absence of the template, one-dimensional array of plasmonic NPs can be produced by spontaneous self-assembly: the colloidal suspension is a metastable system whose stability is determined by a balance between the long-range van der Waals attractions and short-range electrostatic repulsions of the counterions surrounding the NPs (in the present case, the PAA). (19−24,53,54) In the present study, the pH of the solutions is very close to the pKa of the acrylic acid (pKa = 4.25) so the ionization of the carboxylate ion versus the hydrogenated acid form is equilibrated and decreases, whereas pH is decreasing allowing the chain formation until the point where the interactions are too strong and induce the complete precipitation.

The measured ellipsometric spectra of suspensions are reported in Figure 2. The plasmon bands are clearly observed in the 525–650 nm spectral range of the Ic spectra, confirming that ellipsometry is sufficiently sensitive to detect the Au NPs.

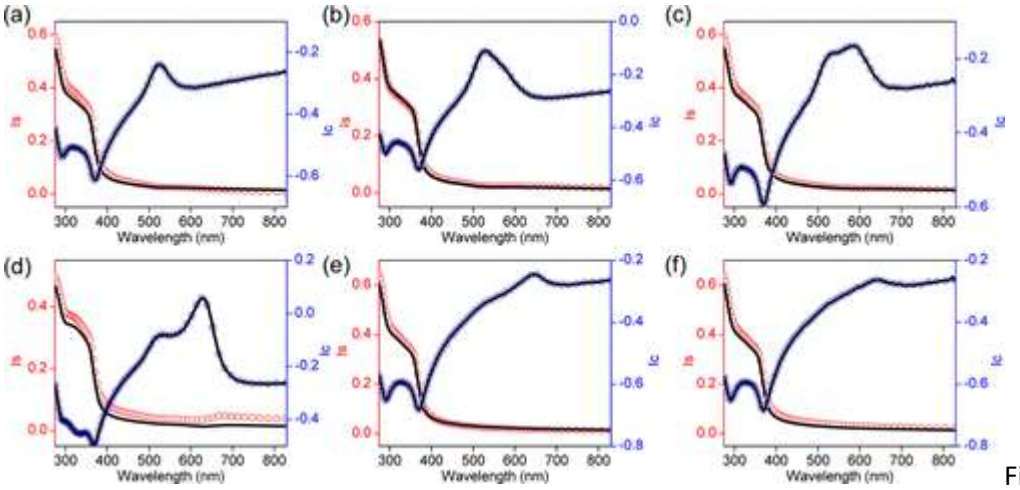

Figure 2

Figure 2. Measured ellipsometric spectra (dots) of (a) S1, (b) S2, (c) S3, (d) S4, (e) S5, and (f) S6 solutions. The blue and red dots show the Ic and Is measured spectra of suspensions, respectively. The ellipsometric spectra calculated from a wavelength-by-wavelength inversion are also represented as solid black lines.

As shown in Figure 2, the ellipsometric measurements are well-reproduced by the wavelength-by-wavelength inversion. The effective refractive index and extinction coefficient of the suspensions, deduced from the wavelength-by-wavelength inversion of ellipsometric measurements, are depicted in Figures S3 and 3, respectively. The effective refractive index of the suspensions is close to the refractive index of water (55) used as a solvent. Small deviations between the measured refractive index and the tabulated refractive index of water can be attributed to the presence of the PAA polymer, and the chemical residue (sodium tricitrate, HCl, and NaOH) used during the NP chain synthesis. In contrast, the interband transitions located below 500 nm and the plasmon bands of Au NPs are clearly distinguished in the effective extinction coefficient of suspensions (Figure 3). The extinction coefficient spectra of S1 are dominated by a single plasmon band located at 521 nm. This band is also observed in the extinction coefficient spectra of other suspensions, whereas a second band appears at higher wavelength. This latter is red shifted from 559 to 646 nm as the pH decreases. According to several authors, (56−58) this splitting of the plasmon band is a consequence of the asymmetric interactions between NPs. Indeed, straight linear chain of coupled NPs exhibits two bright plasmon modes. (56−58)

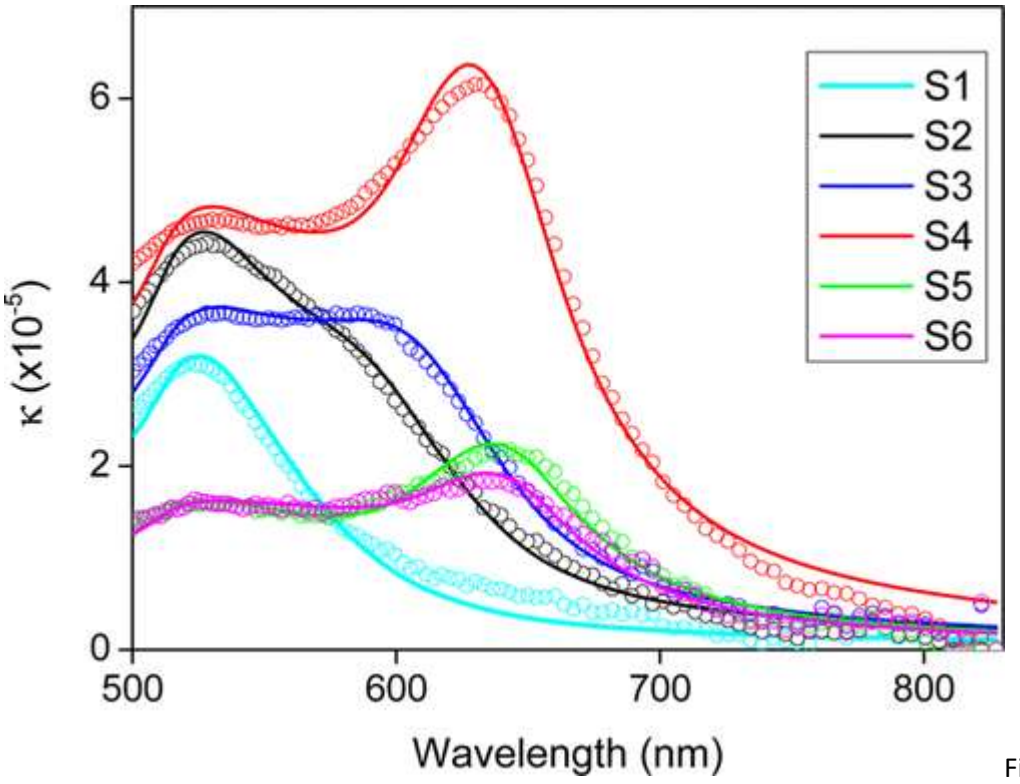

Figure 3

Figure 3. Comparison between the effective extinction coefficient spectra of colloidal suspensions measured by ellipsometry and the calculated ones by CDM.

Modeling

The effect of various parameters on the optical cross section of NP chains was investigated by using the CDM.

Interparticle Distance

The influence of the interparticle distance on the optical properties of NP chains is investigated by simulating the extinction coefficient of a straight linear chain in water. These chains are composed of five Au NPs with a radius of 7 nm. In the following, the interparticle distance d is defined as the distance between the centers of adjacent particles. This latter is related to the interparticle gap g and NP radius R by d = g + 2R. As it is shown in Figure 4, for interparticle distance higher than 17 nm (i.e., interparticle gap g > 3 nm), the extinction coefficient spectra of NP chain are similar to the one of the isolated sphere. The spectra exhibit a narrow plasmon band centered at 525 nm. As highlighted in Figure 4b and in accordance with the measured effective extinction coefficient of suspensions (Figure 3), the plasmon band is splitted into two bands for interparticle distance smaller than 17 nm: the longitudinal (L-SPR) and transversal (T-SPR) plasmon bands. This splitting is a consequence of the coupling effect in an anisotropic assembly of NPs. (56−58) As suggested in Figure 4b, the longitudinal plasmon mode (L-SPR) is selectively excited when the incident electric field is parallel to the NP chains. (56−58) According to several authors, (18,22) the L-SPR mode observed here is a super-radian resonance, that is, all dipoles in the chains oscillate in the phase. In this case, the NPs are polarized, such that, the induced local electric field is in the same direction as the applied field. The restoring force applied on the electron cloud is reduced and the plasmon band is red-shifted. (56−58) In

contrast, the transversal plasmon mode (T-SPR) is excited when the incident electric field is perpendicular to the NP chains. The induced local electric field points in the opposite direction as the applied field. The restoring force applied on the electron cloud is enhanced, and the plasmon band is blue shifted. (56−58)

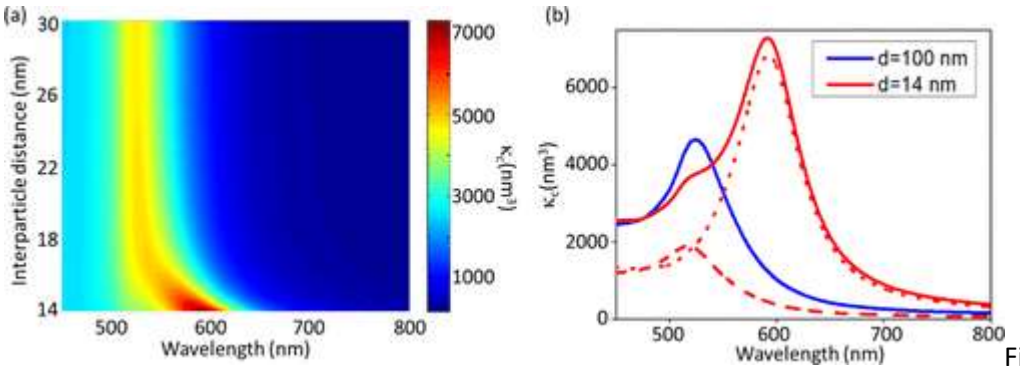

Figure 4

Figure 4. (a) Evolution of the simulated effective extinction coefficient spectra of chains with the interparticle distance. These simulations are made by considering unpolarized light. (b) Effective extinction coefficient spectra of NP chains, which exhibit an interparticle distance of 100 nm (blue lines) and 14 nm (red lines). The spectra are calculated for unpolarized light (solid lines), and a linear polarization parallel (dots) and perpendicular (dash lines) to the NP chains. The straight chains are composed of 5 NPs with a 7 nm radius. Water is used as a matrix.

The amplitude of the T-SPR plasmon band is smaller than the L-SPR one (Figure 4). Despite the interparticle distance has a negligible effect on the position of the transversal plasmon band, a decrease of the interparticle distance induces a pronounced red shift of the L-SPR band. Indeed, the more interparticle distance decreases, the more NPs are coupled, reducing the restoring force applied on the electron cloud. (58) In the conductive contact limit, multipolar interaction and quantum effect such as charge-transfer plasmon or tunneling effect become significant. (41−45) Our CDM cannot capture these effects. Thus, much more appropriate approaches such as time-dependent local density approximation or quantum-corrected model (39,40) must be used to simulate the optical properties of these NPs. However, these approaches are too time-consuming and require too large computing resources to be applied for long NP chains. In our case, cryoTEM images (Figure S2) reveal that the gap between NPs (interparticle gap, g) is close to 1 nm. As shown in Figure 4, the extinction coefficient spectra of NP chains, which have an interparticle gap of 1 nm, are close to the one of the chain composed of NPs in conducting contact. Thus, we consider in the following that the suspension found by point dipole approximation in the conductive contact regime has an asymptotic limit for interparticle gap smaller than 1 nm.

Influence of the Number of NPs in a Chain

To evaluate the influence of the number of NPs in a chain, we have simulated the extinction coefficient spectra of straight linear chains composed of Nnp spherical Au NPs with a 7 nm radius. The adjacent NPs are in conductive contact (g = 0). Figure 5a shows the evolution of the extinction coefficient spectra and the resonance wavelengths with the number of NPs per chain. The optical properties of NP chains can be tuned by changing the number of NPs. Indeed, the T-SPR band is slightly blue shifted, whereas a large red shift is observed for the L-SPR band as the number of NPs in

the chain increases. This red shift of the L-SPR band saturates at about 640 nm for 25–30 NPs, suggesting that the NP assembly can be viewed as an infinite chain. In other words, despite the nearest-neighbor interactions play a major rule, the long-range interactions must be taken into account to describe accurately the optical properties of NP chains. As shown in Figure 5b, the L-SPR wavelength found by ellipsometry is close to the simulated one. Because CDM reproduces the correct L-SPR wavelength in the asymptotic conductive contact limit, it is not unreasonable to exclude quantum effects and multipolar effects. These effects can be viewed as small perturbations and not change the overall conclusions.

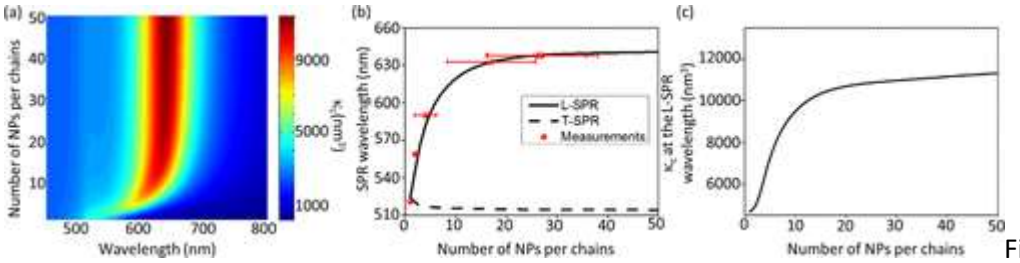

Figure 5

Figure 5. Evolution of (a) simulated effective normalized extinction coefficient spectra, (b) L-SPR and T-SPR wavelengths, and (c) normalized effective extinction resonance at the L-SPR wavelength with the number of NPs per chains. The straight chains consist of NPs in asymptotic conductive contact limit. The NP radius is 7 nm, and water is used as a matrix. The measured L-SPR wavelength by ellipsometry as a function of the mean number of NPs per chains estimated by TEM is also reported in (b).

Figure 5c reveals that the amplitude of the L-SPR band increases with the number of NPs in the chain. As expected, the extinction coefficient is roughly proportional to the number of NPs for infinite chain length limit. Indeed, κc remains nearly constant for the number of NPs per chains higher than 25 NPs. However, this scaling law fails for smaller number of NPs, confirming that NPs cannot be considered as isolated absorption center and plasmon hybridization occurs between them.

Influence of Ramification of NPs in a Chain

As shown in TEM images (Figure 1), long NP chains, such as observed in S4, S5, and S6, exhibit some ramifications. The effect of ramifications on the extinction coefficient of NP chains was investigated by considering the chain structure depicted in Figure S4a. This structure consists of M1-aligned NPs connected to two symmetrical branches which contain M2 NPs. The angle θ between these branches varies in the 60°–180° range. The extinction coefficient spectra of these structures are simulated by considering the asymptotic conductive contact limit. Three sets of (M1, M2) values are considered: (5, 5), (3, 3), and (5, 3). The NP radius is 7 nm, and water is used as a matrix. The simulated extinction coefficient spectra, shown in Figures S4 and 6a, reveal that the T-LSPR band and interband transitions are independent of the angle between the branches. An increase of this angle only induces a small shift and a decrease of the amplitude of the L-SPR band. Compared to the high sensitivity of the L-SPR band to the number of NPs and interparticle distance, we conclude that the angle between branches has a negligible effect on the optical properties of ramified chains. The extinction coefficient spectra of a ramified structure are close to the spectra of a straight linear chain composed of the same number of NPs as the longest path of the ramified chain. In other words, the spectra are dominated by the hybridization of the plasmon mode along the longest NP subchain. (21)

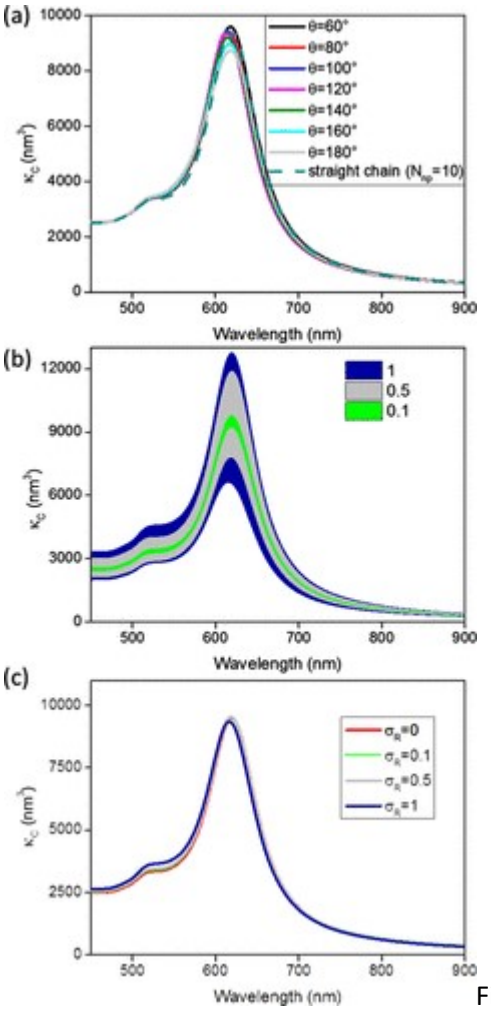

Figure 6

Figure 6. (a) Evolution of the extinction coefficient spectra with the angle between ramifications of (5, 5) ramified chain. The spectra of straight linear chain composed of 10 NPs are also reported. (b) Influence of the standard deviation σR of the NP radius distribution on the range, in which the extinction coefficient of each individual NP straight chain, taken separately, can vary and (c) on the extinction coefficient of suspensions composed of these chains. The NP mean radius used for the simulations is 7 nm. The number of NPs per chains is 10. The simulations are performed by considering NPs in asymptotic conductive contact limit.

Effect of NP Size Distributions

As shown in TEM images (Figure 1) and size distribution (Figure S1), NPs exhibit some polydispersity in radius of about ±10%. Therefore, we investigated the effect of such polydispersity on the optical properties of linear chains. To introduce this polydispersity in the simulations, the NP radius was randomly generated from a Gaussian distribution with a mean value of 7 nm and a standard deviation σR in the 0–1 nm range. Simulations are made for 100 randomly generated linear chains composed of 2, 5, 10, and 20 NPs in asymptotic conductive contact limit. Figures 6b and S5 show the range in which the extinction coefficient of each individual NP chain, taken separately, can vary. Each generated NP chain has its own optical signature. Indeed, the range in which the extinction coefficient of each NP chain can vary, increases as the standard deviation increases. However, the

SPR wavelength does not depend on the NP size in the chain. As reported by Jain et al. for small NP radius, the SPR wavelength is invariant for constant ratio $R/r_{m,m+1}$ between the NP radius R and the distance $r_{m,m+1}$ between two adjacent NPs. (58) Note that in these simulations, this ratio is equal to 2. Indeed, the SPR wavelength is defined by two competing forces: the near-field interaction and the restoring force applied on the electron cloud. The restoring force, which is related to the inverse of the NP polarizability, scales as the inverse of R^3. According to eq 6, the near-field interaction decays as $r_{m,m+1}^{-3}$. Thus, the coupling strength is a function of the ratio $R/r_{m,m+1}$. A distribution of NP radius in the chain only changes the overall magnitude of the extinction coefficient of isolated chains. As each chain exhibits a specific extinction coefficient, an increase of the standard deviation of NP radius induces a broadening of the distribution of extinction coefficient. This broadening is more pronounced for shorter chain length. Indeed, the NP size distribution induces variations of polarizability of the NPs in the chain. Because of the NP coupling, these local variations can be averaged in long NP chains.

The extinction spectra of colloidal suspensions, which contain chains of NPs distributed in radius, are shown in Figures 6c and S6. These spectra are calculated by averaging the contribution of all individual chains. Despite the high sensitivity of the optical response of individual chains to the NP size distribution, this latter has a negligible effect on the optical properties of colloidal suspensions. Thus, spectroscopic measurements performed on a collection of NPs blind the spectral variations between chains induced by the NP size distribution.

Disorder of NPs in the Chain

TEM images (Figure 1) reveal that long chains are not straight and present a degree of disorder, that is, NPs have random position in the chain. To evaluate the effect of the disorder on the optical properties of suspensions, we have introduced the disorder in the linear chain of NPs. Chains are composed of 3, 5, 10, and 20 Au NPs in asymptotic conductive contact limit. Their radius is set at 7 nm. The disordered chains are built as following. As shown in Figure 7a, we can define an orthonormal local frame $(e1,(l,l+1),e2,(l,l+1),e3,(l,l+1))$ for each pair of adjacent NPs (l and l + 1). The basis vector $e1,(l,l+1)$ is collinear to the (l,l + 1) pair of NPs. The position of the subsequent (l + 2) NP can be obtained by using two angles $(\theta_{l+2}, \phi_{l+2})$ defined as the spherical coordinates of the NP (l + 2) in a local frame $(e1,(l,l+1),e2,(l,l+1),e3,(l,l+1))$. These set of angles are equal to (0, 0) for straight linear chains. These angles are randomly generated according to a Gaussian distribution centered on 0. The degree of disorder is given by the standard deviation $\sigma_{\theta,\phi}$ of the distribution. Note that this latter is estimated from TEM images at about 15° (Figure 1). For each chain length and standard deviation, the extinction coefficient spectra of 100 chains are simulated. The extinction coefficient spectra of colloidal suspensions composed of disordered chains, shown in Figure 7, are then calculated by averaging the spectra of all individual chains. The main characteristics of straight chain spectra are preserved. Indeed, two SPR bands can be clearly observed in disordered chains. The extinction coefficient in the interband transitions spectral range is not sensitive to the disorder. In addition, the disorder slightly reduces the amplitude of the T-L-SPR band. As reported by Esteban et al., (21) the L-SPR is blue shifted and its amplitude decreases as the degree of disorder increases. These variations are more pronounced for the longest NP chains. Indeed, straight linear chains support two plasmon modes, which can be selectively excited by a polarization parallel and perpendicular to the chain axis. As disorganized chains are not perfectly straight, the excitation of these modes is less effective, decreasing the amplitude of the plasmon modes. In addition, for an incident electric field parallel to the NP chain, the restoring force applied on the electron cloud is less reduced for disorganized chain than that for the straight chain. Thus, the L-SPR band of disorganized chain is blue shifted. (21)

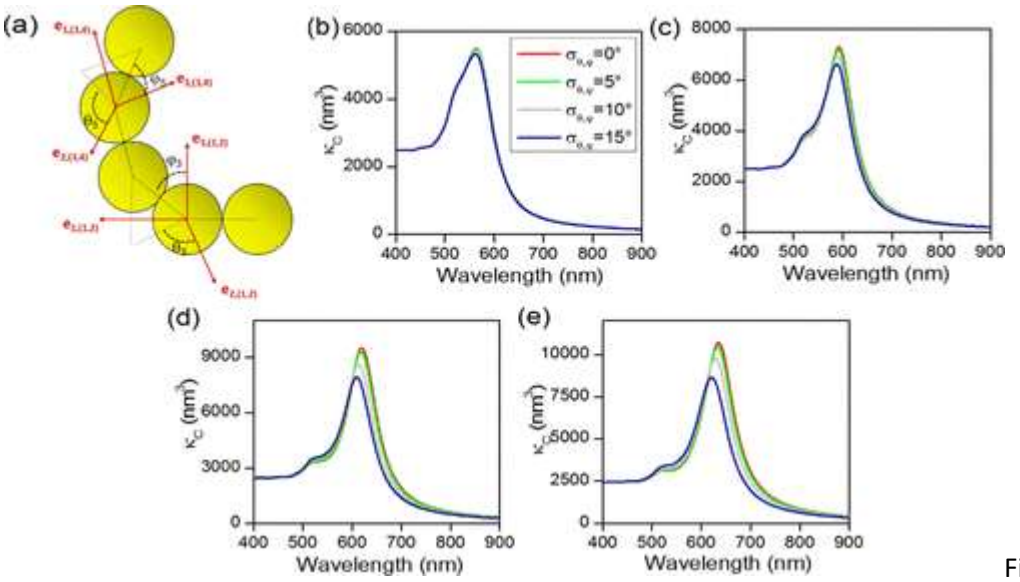

Figure 7

Figure 7. (a) Schematic representation of disordered chains of NPs. (c–e) Influence of the standard deviation σθ,ϕ on the extinction coefficient of suspensions which contain NP chains. The simulations are performed by considering chains composed of (b) 2, (c) 5, (d) 10, and (e) 20 NPs in conductive contact limit. The radius of NP is 7 nm, and water is used as a matrix.

NP Loop in the NP Chain

TEM images (Figure 8a) reveal that long NP chains (samples S5 and S6) exhibit some closed loops and complex ramifications. To investigate the effect of closed loop on the optical properties of chains, we have simulated the extinction coefficient spectra of an assembly of 10 NPs, in conductive contact limit, organized into a circle. The extinction coefficient spectra of this NP ring, shown in Figure 8, are compared to one of a straight linear chain composed of 10 NPs. Because of its symmetry, the ring supports two plasmon modes: an in-plane plasmon mode which can be selectively excited by an incident light with a polarization parallel to the ring plane and an out-of-plane plasmon mode which can be selectively excited with a polarization perpendicular to the ring plane (Figure 8a). The plasmon bands assigned to the in-plane and out-of-plane plasmon modes are centered at 573 and 514 nm, respectively. Under unpolarized light, the spectra of the ring are dominated by the in-plane plasmon mode. The in-plane plasmon mode of the NP ring is blue shifted by 45 nm with respect to the L-SPR plasmon band of straight linear chains composed of 10 NPs. According to Figure 5, the position of the in-plane plasmon band is similar to one of the L-SPR mode of straight linear chains, which contain 3 NPs. Thus, the optical properties of rings are less sensitive to the number of NPs than straight chains. In addition, the in-plane plasmon band of ring has smaller amplitude of the L-SPR plasmon band of straight chain.

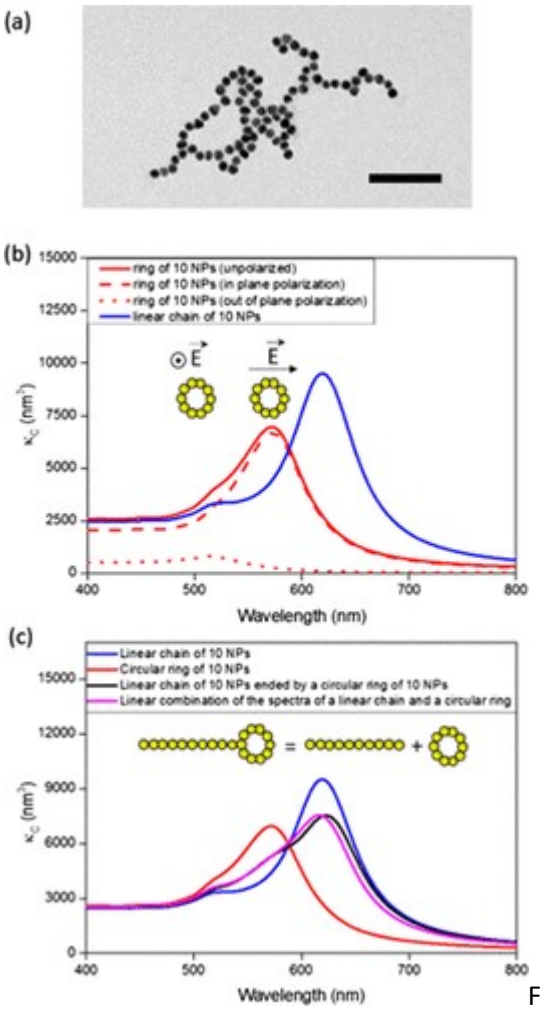

Figure 8

Figure 8. (a) TEM image of a Au NP chain ramified and forming loops (sample S5). The scale bar is 100 nm. (b) Comparison between the extinction coefficient spectra of 10 NPs organized into a ring (red solid line) and 10 NPs organized into a straight linear chain (blue solid line) exposed to unpolarized light. The extinction coefficient spectra of a ring calculated for in-plane (red dashed line) and out-of-plane (red dotted line) linear polarizations are also reported. (c) Extinction coefficient spectra of a straight linear chain of 10 NPs (blue solid line), a circular ring of 10 NPs (red solid line), and a straight linear chain of 10 NPs ended by a circular ring of 10 NPs (black solid line). The simulations are performed for unpolarized incident light. In pink solid line, the spectra obtained from a linear combination between the spectra of straight linear chain of 10 NPs and the spectra of a circular ring of 10 NPs. The NPs are in conductive contact limit. Their radius is 7 nm.

To give a more complete description of chains which contained closed loop, we have also simulated the extinction coefficient spectra of an assembly of 20 NPs in water, which consists of 10 NPs organized in a straight linear chain ended by 10 NPs organized in a circular ring. The NPs, whose radius is set to 7 nm, are in conductive contact limit. As shown in Figure 8, three plasmon bands, located at 623, 573, and 520 nm, are observed in the extinction coefficient spectra. The band located at 623 nm has the highest amplitude. In a first approximation, the extinction coefficient spectra of this structure can be deduced from a linear combination of the extinction coefficient spectra of two NP assemblies: a straight linear chain composed of 10 NPs and a circular ring composed of 10 NPs. In

other words, the optical properties of NP chain which contained closed loop are simultaneously sensitive to both: linear sub-branch and the NP rings.

Determination of the Distribution of the Number of NPs per Chains from Ellipsometry

As we discussed above, simulations have shown that the optical properties of NP chains are mainly sensitive to the interparticle distance and to the number of NPs in chains. Meanwhile, as shown in Figures 1 and 5, the interparticle distance in the synthesized chains is sufficiently small to be simulated as having asymptotic conductive contact limit. Thus, in the following, the CDM is used to estimate the distribution of number of NPs in chains from the effective extinction coefficient of suspensions measured by ellipsometry.

This analysis is performed by using the following procedure. First, the extinction coefficient spectra of several straight linear chains composed of Nnp Au NPs in the asymptotic conductive contact limit are calculated from the CDM. The number of NPs in the chain varies from 1 to 60. The NP radius is set to 7 nm, that is, the measured mean radius from TEM. In accordance with Figure 6c, the distribution of NP radius can be neglected. The real part of refractive index of the suspension found by ellipsometry is used as the refractive index of the matrix. This latter, which depends on the nature of the solvent and the presence of chemical species (PAA, HCl, and NaOH) used to synthesize the NP chains, is directly introduced in the CDM to calculate κc. In other words, the determination of the refractive index of the matrix is crucial for our model. Indeed, an inaccurate effective refractive index of the matrix leads to an inaccurate distribution of the number of NP per chains. This parameter cannot be deduced from other techniques such as absorption spectroscopy, suggesting that ellipsometric measurements must be used to characterize the optical properties and the composition of NP chains. The effective extinction spectra of suspension are then calculated by weighting κc(Nnp) of individual chains by the distribution of the number of NPs per chains:

$$\kappa = \frac{3}{4\pi R^3} \sum_{N_{np}=1}^{Npmax} P_f(N_{np}) \kappa_c(N_{np}) \quad (19)$$

Pf(Nnp) is the volume fraction distribution of chains composed of Nnp NPs with a radius R. We assume that Pf(Nnp) is described as a sum of two Gaussian distributions

$$P_f(N) = \sum_{i=1}^{2} A_i \, e^{-0.5(N_{np} - \overline{N_{np,i}}/\sigma_i)^2} \quad (20)$$

Ai, , and σi are the amplitude, the mean value, and the standard deviation of the Gaussian distribution i, respectively. These parameters are fitted by minimizing the root-mean-square error between the measured and the calculated effective extinction coefficient spectra by the Levenberg–Marquardt algorithm. (51) Because the interband transitions of Au are weakly sensitive to the number of NPs per chains, we restrict the analysis to the 500–800 nm spectral range. The correlation matrix (not shown) reveals that all fitted parameters are independent. The comparison between the measured and calculated effective extinction coefficient spectra, shown in Figure 3, confirms that the CDM reproduces the optical properties of suspensions.

The distributions of number of NPs per chains obtained from ellipsometry, shown in Figure 9, are compared with the ones estimated by TEM (Figure 1). According to simulations performed on ramified chains, this comparison suggests that the distributions obtained by ellipsometry can be assimilated to the distributions of the number of NPs contained in the longest segment of chains. Indeed, the mean values of the distributions of number of NPs per chains are reproduced. Meanwhile, the S5 and S6 distributions deduced from ellipsometry suggest that these suspensions

are composed of two populations of NP chains: one of the populations is the long chains composed of 25–40 NPs. The other population is either short NP chains or the loops as both types of structures give contribution to the extinction coefficient spectra in the same spectral range, as shown in Figure 8. As we observe form TEM images, this contribution is more likely induced by the loops rather than the short linear chains composed of 1–5 NPs.

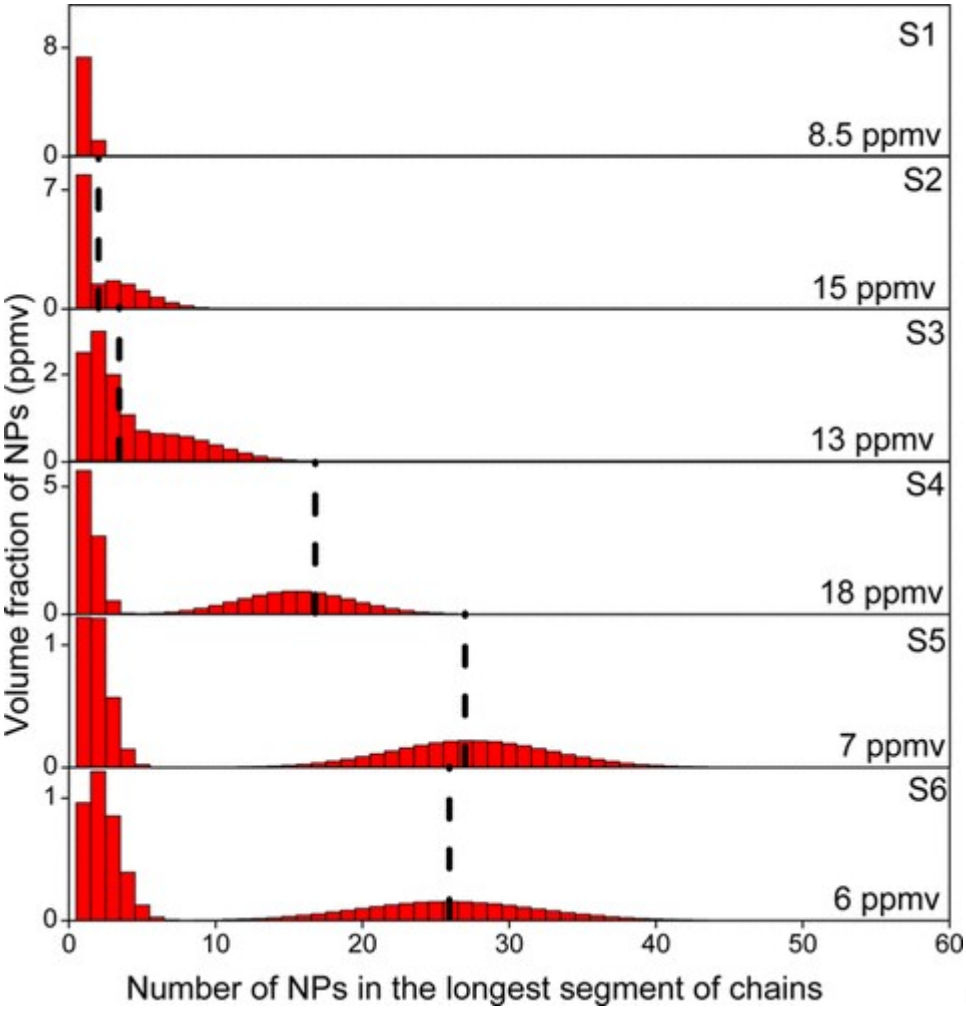

Figure 9

Figure 9. Distribution of the number of NPs in the longest segment of chains obtained from ellipsometry. The estimated volume fractions of chains are also reported.

The knowledge of the refractive index of the matrix, which constitutes a key point for the quantitative analysis of optical spectra, prevents the use of absorption spectroscopy for the characterization of the NP chain length. Thus, the method developed here takes the advantage of the sensitivity of ellipsometric measurements to both the real part and the imaginary part of the complex refractive index of materials. On contrary to TEM, ellipsometry is a nonlocal characterization tool. By considering the volume fraction of NP chains as well as the ellipsometric cell spacer and beam diameter, the number of probed chains is estimated at 1010. This suggests that the number of probed NPs by ellipsometry is sufficiently significant to give an accurate estimation of the distribution of the number of NP per chains. In addition, on contrary to TEM, ellipsometry can be used to give a quantitative estimation of the volume fraction of chains in the suspension. This latter, reported in

Figure 9, is in the 6–18 ppmv range, confirming that the chains are sufficiently diluted to neglect the interchain interaction.

Conclusions

In summary, spectroscopic ellipsometry is used to determine the optical properties of suspensions composed of Au NP chains. The real and imaginary parts of the effective refractive index of these suspensions mainly depend on the refractive index of the solvent and the plasmonic properties of the NP chains, respectively. CDM introduced to explain the impact of the morphology of NP chains on their optical properties reveals that the position of the L-SPR band depends on the number of NP in the longest segment of NP chain as well as the interparticle distance. This model, which does not take into account multipolar and quantum effects, remarkably reproduces the measured spectra. We demonstrate that the distributions of the number of NPs in the longest segment of chains as well as their volume fraction can be determined from effective extinction coefficient spectra by fitting it with the CDM, and these distributions are in very good agreement with the ones obtained from TEM measurements. Thus, ellipsometry combined with the CDM successfully provide a detailed image of NP chains in the suspension.

1Kreibig, U.; Vollmer, M. Optical Properties of Metal Clusters; Springer Series in Materials Science; Springer: Berlin 1995.[Crossref], Google Scholar

2Battie, Y.; Resano-Garcia, A.; Chaoui, N.; Zhang, Y.; En Naciri, A. Extended Maxwell-Garnett-Mie Formulation Applied to Size Dispersion of Metallic Nanoparticles Embedded in Host Liquid Matrix. J. Chem. Phys. 2014, 140, 044705, DOI: 10.1063/1.4862995 [Crossref], [PubMed], [CAS], Google Scholar

3Battie, Y.; Resano-Garcia, A.; En Naciri, A.; Akil, S.; Chaoui, N. Determination of Morphological Characteristics of Metallic Nanoparticles Based on Modified Maxwell-Garnett Fitting of Optical Responses. Appl. Phys. Lett. 2015, 107, 143104, DOI: 10.1063/1.4932638 [Crossref], Google Scholar

4Resano-Garcia, A.; Battie, Y.; En Naciri, A.; Akil, S.; Chaoui, N. Experimental and Theoretical Determination of the Plasmonic Responses and Shape Distribution of Colloidal Metallic Nanoparticles. J. Chem. Phys. 2015, 142, 134108, DOI: 10.1063/1.4916917 [Crossref], [PubMed], [CAS], Google Scholar

5González, A. L.; Noguez, C. Influence of Morphology on the Optical Properties of Metal Nanoparticles. J. Comput. Theor. Nanosci. 2007, 4, 231– 238, DOI: 10.1166/jctn.2007.2309 [Crossref], [CAS], Google Scholar

6Kelly, K. L.; Coronado, E.; Zhao, L. L.; Schatz, G. C. The Optical Properties of Metal Nanoparticles: the Influence of Size, Shape, and Dielectric Environment. J. Phys. Chem. B 2003, 107, 668– 677, DOI: 10.1021/jp026731y [ACS Full Text ACS Full Text], [CAS], Google Scholar

7Alvarez-Puebla, R.; Liz-Marzán, L. M.; de Abajo, F. J. G. Light Concentration at the Nanometer Scale. J. Phys. Chem. Lett. 2010, 1, 2428– 2434, DOI: 10.1021/jz100820m [ACS Full Text ACS Full Text], [CAS], Google Scholar

8Forestiere, C.; Pasquale, A. J.; Capretti, A.; Miano, G.; Tamburrino, A.; Lee, S. Y.; Reinhard, B. M.; Dal Negro, L. Genetically Engineered Plasmonic Nanoarrays. Nano Lett. 2012, 12, 2037– 2044, DOI: 10.1021/nl300140g [ACS Full Text ACS Full Text], [CAS], Google Scholar

9Ross, M. B.; Mirkin, C. A.; Schatz, G. C. Optical Properties of One-, Two-, and Three-Dimensional Arrays of Plasmonic Nanostructures. J. Phys. Chem. C 2016, 120, 816– 830, DOI: 10.1021/acs.jpcc.5b10800 [ACS Full Text ACS Full Text], [CAS], Google Scholar

10Cheng, J.; Le Saux, G.; Gao, J.; Buffeteau, T.; Battie, Y.; Barois, P.; Ponsinet, V.; Delville, M.-H.; Ersen, O.; Pouget, E.GoldHelix: Gold Nanoparticles Forming 3D Helical Superstructures with Controlled Morphology and Strong Chiroptical Property. ACS Nano 2017, 11, 3806– 3818, DOI: 10.1021/acsnano.6b08723 [ACS Full Text ACS Full Text], [CAS], Google Scholar

11Song, C.; Blaber, M. G.; Zhao, G.; Zhang, P.; Fry, H. C.; Schatz, G. C.; Rosi, N. L. Tailorable Plasmonic Circular Dichroism Properties of Helical Nanoparticle Superstructures. Nano Lett. 2013, 13, 3256– 3261, DOI: 10.1021/nl4013776 [ACS Full Text ACS Full Text], [CAS], Google Scholar

12Wang, L.; Deng, L. Plasmonic Circular Dichroism of the Helical Nanosphere Assemblies and the Helical Nanoellipsoid Assemblies. Plasmonics 2015, 10, 399– 409, DOI: 10.1007/s11468-014-9821-1 [Crossref], [CAS], Google Scholar

13Hentschel, M.; Dregely, D.; Vogelgesang, R.; Giessen, H.; Liu, N. Plasmonic Oligomers: The Role of Individual Particles in Collective Behavior. ACS Nano 2011, 5, 2042– 2050, DOI: 10.1021/nn103172t [ACS Full Text ACS Full Text], [CAS], Google Scholar

14Hentschel, M.; Saliba, M.; Vogelgesang, R.; Giessen, H.; Alivisatos, A. P.; Liu, N. Transition from Isolated to Collective Modes in Plasmonic Oligomers. Nano Lett. 2010, 10, 2721– 2726, DOI: 10.1021/nl101938p [ACS Full Text ACS Full Text], [CAS], Google Scholar

15Yan, B.; Boriskina, S. V.; Reinhard, B. M. Design and Implementation of Noble Metal Nanoparticle Cluster Arrays for Plasmon Enhanced Biosensing. J. Phys. Chem. C 2011, 115, 24437– 24453, DOI: 10.1021/jp207821t [ACS Full Text ACS Full Text], [CAS], Google Scholar

16Fan, J. A.; Wu, C.; Bao, K.; Bao, J.; Bardhan, R.; Halas, N. J.; Manoharan, V. N.; Nordlander, P.; Shvets, G.; Capasso, F. Self-Assembled Plasmonic Nanoparticle Clusters. Science 2010, 328, 1135– 1138, DOI: 10.1126/science.1187949 [Crossref], [PubMed], [CAS], Google Scholar

17Greybush, N. J.; Liberal, I.; Malassis, L.; Kikkawa, J. M.; Engheta, N.; Murray, C. B.; Kagan, C. R. Plasmon Resonances in Self-Assembled Two-Dimensional Au Nanocrystal Metamolecules. ACS Nano 2017, 11, 2917– 2927, DOI: 10.1021/acsnano.6b08189 [ACS Full Text ACS Full Text], [CAS], Google Scholar

18Brandl, D. W.; Mirin, N. A.; Nordlander, P. Plasmon Modes of Nanosphere Trimers and Quadrumers. J. Phys. Chem. B 2006, 110, 12302– 12310, DOI: 10.1021/jp0613485 [ACS Full Text ACS Full Text], [CAS], Google Scholar

19Barrow, S. J.; Funston, A. M.; Gómez, D. E.; Davis, T. J.; Mulvaney, P. Surface Plasmon Resonances in Strongly Coupled Gold Nanosphere Chains from Monomer to Hexamer. Nano Lett. 2011, 11, 4180– 4187, DOI: 10.1021/nl202080a [ACS Full Text ACS Full Text], [CAS], Google Scholar

20Li, Z.; Butun, S.; Aydin, K. Touching Gold Nanoparticle Chain Based Plasmonic Antenna Arrays and Optical Metamaterials. ACS Photonics 2014, 1, 228– 234, DOI: 10.1021/ph4000828 [ACS Full Text ACS Full Text], Google Scholar

21Esteban, R.; Taylor, R. W.; Baumberg, J. J.; Aizpurua, J. How Chain Plasmons Govern the Optical Response in Strongly Interacting Self-Assembled Metallic Clusters of Nanoparticles. Langmuir 2012, 28, 8881– 8890, DOI: 10.1021/la300198r [ACS Full Text ACS Full Text], [CAS], Google Scholar

22Slaughter, L. S.; Willingham, B. A.; Chang, W.-S.; Chester, M. H.; Ogden, N.; Link, S. Toward Plasmonic Polymers. Nano Lett. 2012, 12, 3967– 3972, DOI: 10.1021/nl3011512 [ACS Full Text ACS Full Text], [CAS], Google Scholar

23Lin, S.; Li, M.; Dujardin, E.; Girard, C.; Mann, S. One-Dimensional Plasmon Coupling by Facile Self-Assembly of Gold Nanoparticles into Branched Chain Networks. Adv. Mater. 2005, 17, 2553– 2559, DOI: 10.1002/adma.200500828 [Crossref], [CAS], Google Scholar

24Zou, S.; Janel, N.; Schatz, G. C. Silver Nanoparticle Array Structures That Produce Remarkably Narrow Plasmon Lineshapes. J. Chem. Phys. 2004, 120, 10871– 10875, DOI: 10.1063/1.1760740 [Crossref], [PubMed], [CAS], Google Scholar

25Huang, Y.; Zhou, Q.; Hou, M.; Ma, L.; Zhang, Z. Nanogap Effects on Near- and Far-Field Plasmonic Behaviors of Metallic Nanoparticle Dimers. Phys. Chem. Chem. Phys. 2015, 17, 29293– 29298, DOI: 10.1039/c5cp04460j [Crossref], Google Scholar

26Wang, Z. B.; Luk'yanchuk, B. S.; Guo, W.; Edwardson, S. P.; Whitehead, D. J.; Li, L.; Liu, Z.; Watkins, K. G. The Influences of Particle Number on Hot Spots in Strongly Coupled Metal Nanoparticles Chain. J. Chem. Phys. 2008, 128, 094705, DOI: 10.1063/1.2835598 [Crossref], Google Scholar

27Chen, G.; Wang, Y.; Yang, M.; Xu, J.; Goh, S. J.; Pan, M.; Chen, H. Measuring Ensemble-Averaged Surface-Enhanced Raman Scattering in the Hotspots of Colloidal Nanoparticle Dimers and Trimers. J. Am. Chem. Soc. 2010, 132, 3644– 3645, DOI: 10.1021/ja9090885 [ACS Full Text ACS Full Text], [CAS], Google Scholar

28Brongersma, M. L.; Hartman, J. W.; Atwater, H. A. Electromagnetic Energy Transfer and Switching in Nanoparticle Chain Arrays Below the Diffraction Limit. Phys. Rev. B: Condens. Matter Mater. Phys. 2000, 62, R16356– R16359, DOI: 10.1103/physrevb.62.r16356 [Crossref], Google Scholar

29Willingham, B.; Link, S. Energy Transport in Metal Nanoparticle Chains via Sub-Radiant Plasmon Modes. Opt. Express 2011, 19, 6450– 6461, DOI: 10.1364/oe.19.006450 [Crossref], Google Scholar

30Maier, S. A.; Kik, P. G.; Atwater, H. A. Observation of Coupled Plasmon-Polariton Modes in Au Nanoparticle Chain Waveguides of Different Lengths: Estimation of Waveguide Loss. Appl. Phys. Lett. 2002, 81, 1714– 1716, DOI: 10.1063/1.1503870 [Crossref], [CAS], Google Scholar

31Punj, D.; Regmi, R.; Devilez, A.; Plauchu, R.; Moparthi, S. B.; Stout, B.; Bonod, N.; Rigneault, H.; Wenger, J. Self-Assembled Nanoparticle Dimer Antennas for Plasmonic-Enhanced Single-Molecule Fluorescence Detection at Micromolar Concentrations. ACS Photonics 2015, 2, 1099– 1107, DOI: 10.1021/acsphotonics.5b00152 [ACS Full Text ACS Full Text], [CAS], Google Scholar

32Han, X.; Liu, Y.; Yin, Y. Colorimetric Stress Memory Sensor Based on Disassembly of Gold Nanoparticle Chains. Nano Lett. 2014, 14, 2466– 2470, DOI: 10.1021/nl500144k [ACS Full Text ACS Full Text], [CAS], Google Scholar

33Taylor, R. W.; Esteban, R.; Mahajan, S.; Coulston, R.; Scherman, O. A.; Aizpurua, J.; Baumberg, J. J. Simple Composite Dipole Model for the Optical Modes of Strongly-Coupled Plasmonic Nanoparticle Aggregates. J. Phys. Chem. C 2012, 116, 25044– 25051, DOI: 10.1021/jp308986c [ACS Full Text ACS Full Text], [CAS], Google Scholar

34Xu, Y.-L. Electromagnetic Scattering by an Aggregate of Spheres. Appl. Opt. 1995, 34, 4573– 4588, DOI: 10.1364/ao.34.004573 [Crossref], [PubMed], [CAS], Google Scholar

35Myroshnychenko, V.; Rodríguez-Fernández, J.; Pastoriza-Santos, I.; Funston, A. M.; Novo, C.; Mulvaney, P.; Liz-Marzán, L. M.; de Abajo, F. J. G. Modelling the Optical Response of Gold Nanoparticles. Chem. Soc. Rev. 2008, 37, 1792– 1805, DOI: 10.1039/b711486a [Crossref], [PubMed], [CAS], Google Scholar

36Zhao, L.; Kelly, K. L.; Schatz, G. C. The Extinction Spectra of Silver Nanoparticle Arrays: Influence of Array Structure on Plasmon Resonance Wavelength and Width. J. Phys. Chem. B 2003, 107, 7343– 7350, DOI: 10.1021/jp034235j [ACS Full Text ACS Full Text], [CAS], Google Scholar

37Portalés, H.; Pinna, N.; Pileni, M.-P. Optical Response of Ultrafine Spherical Silver Nanoparticles Arranged in Hexagonal Planar Arrays Studied by the DDA Method. J. Phys. Chem. A 2009, 113, 4094– 4099, DOI: 10.1021/jp810478r [ACS Full Text ACS Full Text], Google Scholar

38Romero, I.; Aizpurua, J.; Bryant, G. W.; de Abajo, F. J. G. Plasmons in Nearly Touching Metallic Nanoparticles: Singular Response in the Limit of Touching Dimers. Opt. Express 2006, 14, 9988, DOI: 10.1364/oe.14.009988 [Crossref], [PubMed], [CAS], Google Scholar

39Zuloaga, J.; Prodan, E.; Nordlander, P. Quantum Description of the Plasmon Resonances of a Nanoparticle Dimer. Nano Lett. 2009, 9, 887– 891, DOI: 10.1021/nl803811g [ACS Full Text ACS Full Text], [CAS], Google Scholar

40Esteban, R.; Borisov, A. G.; Nordlander, P.; Aizpurua, J. Bridging Quantum and Classical Plasmonics with a Quantum-Corrected Model. Nat. Commun. 2012, 3, 825, DOI: 10.1038/ncomms1806 [Crossref], [PubMed], [CAS], Google Scholar

41Cha, H.; Yoon, J. H.; Yoon, S. Probing Quantum Plasmon Coupling Using Gold Nanoparticle Dimers with Tunable Interparticle Distances Down to the Subnanometer Range. ACS Nano 2014, 8, 8554– 8563, DOI: 10.1021/nn5032438 [ACS Full Text ACS Full Text], [CAS], Google Scholar

42Yang, L.; Wang, H.; Fang, Y.; Li, Z. Polarization State of Light Scattered from Quantum Plasmonic Dimer Antennas. ACS Nano 2016, 10, 1580– 1588, DOI: 10.1021/acsnano.5b07223 [ACS Full Text ACS Full Text], [CAS], Google Scholar

43Wen, F.; Zhang, Y.; Gottheim, S.; King, N. S.; Zhang, Y.; Nordlander, P.; Halas, N. J. Charge Transfer Plasmons: Optical Frequency Conductances and Tunable Infrared Resonances. ACS Nano 2015, 9, 6428– 6435, DOI: 10.1021/acsnano.5b02087 [ACS Full Text ACS Full Text], [CAS], Google Scholar

44Hohenester, U.; Draxl, C. Ab Initio Approach for Gap Plasmonics. Phys. Rev. B: Condens. Matter Mater. Phys. 2016, 94, 165418, DOI: 10.1103/physrevb.94.165418 [Crossref], Google Scholar

45Hohenester, U. Quantum Corrected Model for Plasmonic Nanoparticles: A Boundary Element Method Implementation. Phys. Rev. B: Condens. Matter Mater. Phys. 2015, 91, 205436, DOI: 10.1103/physrevb.91.205436 [Crossref], Google Scholar

46Zhang, H.; Wang, W.; Akinc, M.; Mallapragada, S.; Travesset, A.; Vaknin, D. Assembling and Ordering Polymer-Grafted Nanoparticles in Three Dimensions. Nanoscale 2017, 9, 8710– 8715, DOI: 10.1039/c7nr00787f [Crossref], [PubMed], [CAS], Google Scholar

47 Ellipsometry at the Nanoscale; Losurdo, M., Hingerl, K., Eds.; Springer Science & Business Media, 2013.[Crossref], Google Scholar

48Battie, Y.; Stchakovsky, M.; En Naciri, A.; Akil, S.; Chaoui, N.; Broch, L. Ellipsometry of Colloidal Solutions: New Experimental Setup and Application to Metallic Colloids. Langmuir 2017, 33, 7425– 7434, DOI: 10.1021/acs.langmuir.7b00490 [ACS Full Text ACS Full Text], Google Scholar

49Ji, X.; Song, X.; Li, J.; Bai, Y.; Yang, W.; Peng, X. Size Control of Gold Nanocrystals in Citrate Reduction: The Third Role of Citrate. J. Am. Chem. Soc. 2007, 129, 13939– 13948, DOI: 10.1021/ja074447k [ACS Full Text ACS Full Text], [CAS], Google Scholar

50Schneider, G.; Decher, G. Functional Core/Shell Nanoparticles via Layer-by-Layer Assembly. Investigation of the Experimental Parameters for Controlling Particle Aggregation and for Enhancing Dispersion Stability. Langmuir 2008, 24, 1778– 1789, DOI: 10.1021/la7021837 [ACS Full Text ACS Full Text], [CAS], Google Scholar

51Levenberg, K. Method for the Solution of Certain Problems in Least Squares. Q. Appl. Math. 1944, 2, 164– 168, DOI: 10.1090/qam/10666 [Crossref], Google Scholar

52Johnson, P. B.; Christy, R. W. Optical constants of the noble metals. Phys. Rev. B: Solid State 1972, 6, 4370, DOI: 10.1103/physrevb.6.4370 [Crossref], [CAS], Google Scholar

53Zhang, H.; Wang, D. Controlling the Growth of Charged-Nanoparticle Chains through Interparticle Electrostatic Repulsion. Angew. Chem. 2008, 120, 4048– 4051, DOI: 10.1002/ange.200705537 [Crossref], Google Scholar

54Guerrini, L.; Graham, D. Molecularly-Mediated Assemblies of Plasmonic Nanoparticles for Surface-Enhanced Raman Spectroscopy Applications. Chem. Soc. Rev. 2012, 41, 7085– 7107, DOI: 10.1039/c2cs35118h [Crossref], [PubMed], [CAS], Google Scholar

55Palik, E. D. Handbook of Optical Constants of Solids; Academic Press Handbook Series: New York, 1985.Google Scholar

56Demchuk, A.; Bolesta, I.; Kushnir, O.; Kolych, I. The Computational Studies of Plasmon Interaction. Nanoscale Res. Lett. 2017, 12, 273, DOI: 10.1186/s11671-017-2050-8 [Crossref], [PubMed], [CAS], Google Scholar

57Marhaba, S.; Bachelier, G.; Bonnet, C.; Broyer, M.; Cottancin, E.; Grillet, N.; Lermé, J.; Vialle, J.-L.; Pellarin, M. Surface Plasmon Resonance of Single Gold Nanodimers near the Conductive Contact Limit. J. Phys. Chem. C 2009, 113, 4349– 4356, DOI: 10.1021/jp810405y [ACS Full Text ACS Full Text], Google Scholar

58Jain, P. K.; Huang, W.; El-Sayed, M. A. On the Universal Scaling Behavior of the Distance Decay of Plasmon Coupling in Metal Nanoparticle Pairs: A Plasmon Ruler Equation. Nano Lett. 2007, 7, 2080– 2088, DOI: 10.1021/nl071008a [ACS Full Text ACS Full Text], [CAS], Google Scholar